

Supplemental methods

Generation of transgenic mice and mouse genotyping

Experimental animal protocols and animal procedures were in line with the standard operating procedures. All animals were maintained in a pathogen-free facility, fed a commercial pellet diet and water *ad libitum*.

PCR using DNA from tail biopsies identified the respective genotypes. For PCR analysis, the following primers were designed. TFR2-ex1-fwd: 5'-CGC TGG GTG CTC AAG TTC TA-3'; TFR2-ex2-rev: 5'-CGC GAC AGA CAC TGC ATA AC-3. PCR was carried out for 30 cycles and amplified material was analyzed by electrophoresis in a 1% agarose gel. The wild-type allele gave a 264 bp fragment, the transgenic allele gave a 167 bp fragment.

Dissection of macroscopic tumors and histological analysis

Animals were humanely sacrificed at 6 or 13 months of age. Macroscopic tumors (diameter more than 2 mm) were counted and tumor volume was assessed. Tumors and livers were dissected and cut into two pieces. One part was snap-frozen (for DNA or protein isolation) and the other half was fixed in 4% PFA overnight and then embedded into paraffin. Sections of livers and tumors (3 μ m) were cut and stained with hematoxyline and eosin (H&E) for histological analysis.

Tumors were classified using the following criteria:

Microscopic foci: Lesions of 0.5-2 mm in diameter with apparent morphological changes in a clonal growth pattern and sometimes slight marginal compression with basophilic, clear cell, or eosinophilic cytomorphology.

Borderline lesions: Nodules of more than 2 mm showing no sign of malignancy.

HCC G1: Well-differentiated tumors with trabecular disorganization, malignancy, and well-defined marginal compression.

HCC G2/G3: Moderately- or poorly-differentiated atypical cells, mostly with necrotic tissue.

MRI analysis

The volume of HCCs was determined by MRI in 11- to 13-months-old DEN-treated female mice before the induction of transient telomere dysfunction. Mice were treated with three doses of doxycycline at two-week time intervals after the first imaging to induce transient telomere dysfunction in TTD⁺ mice. Control mice included PBS-treated TTD⁺ mice as well as doxycycline or PBS-treated TTD⁻ mice. A second MRI scan was carried out four weeks after

the last injection at 14 to 16 months of age, 3 months after the first MRI scan. Representative MRI images of one-year-old TTD⁺ and TTD⁻ mice before and after doxycycline treatment.

Protein isolation and western blot

Tumors were minced using a plastic pastille in RIPA buffer (1% Nonidet P-40 substitute, 0,1%SDS, 1xPBS, 0,5% Sodium deoxycholate) supplemented with protease inhibitors (Complete Mini, Roche; 1mM Sodiummetavanadat; 1mM DDT; 1mM Phenylmethylsulfonylfluorid). Protein was separated on a 15% SDS gel and blotted using a PVDF membrane. γ H2AX protein was detected using a mouse monoclonal phospho-Histone H2AX (Ser139) antibody (Millipore) 1:1000 diluted in 5% milk powder in TBS-T. β -Actin antibody (Millipore) was used as loading control a monoclonal antibody. To detect the expression of TRF2 ^{Δ BD Δ M} the antibody (clone 4A794) dilution 1:1000 was used. HRP-conjugated secondary anti-mouse antibody diluted 1:10000 in 5% milk powder in TBS-T was used. The detection was performed using the ECL developing Kit (Millipore) visualized by a chemiluminescence imager.

Immunohistochemistry for γ H2AX

Paraffin sections were de-waxed and rehydrated. For antigen unmasking, a citric acid-based antigen-unmasking solution (Vector) was used. Sections were quenched for endogenous peroxidases with 3% H₂O₂, blocked and processed according to the manufacturer's protocol of the MOM Kit (Vector) using γ H2AX antibody (Millipore; #636). Staining was developed using the Novared substrate and counterstained with hematoxylin.

Array CGH profiling

Genomic DNA was digested with *RSAI/ALUI*. Labeling of digested genomic DNA with Cy3 or Cy5 was performed using a Genomic DNA Labeling Kit (Agilent) according to the manufacturer's instructions and hybridized to a mouse genome CGH 44K microarray (Agilent Technologies). Data were processed by feature extraction and DNA Analytics 4.0.76. All fluorescence intensities were converted to log₂ values to equally weight gains and losses.

PCNA Staining

Paraffin-embedded sections were de-paraffinized, re-hydrated, and unmasked in a citric acid buffer. Incubation with the primary antibody (PCNA Ab-1, Oncogene Science) was carried

out overnight. Cy3-labeled rabbit anti-mouse antibody was used for the detection of PCNA-positive cells per low power field (200x).

Quantitative fluorescence in situ hybridization (qFISH)

Telomere length was measured by quantitative fluorescence in situ hybridization (qFISH) using paraffin-embedded tumor or liver samples. After unmasking, slides were incubated in pepsine solution and washed. A hybridization mix containing a PNA probe (5-Cy3-CCCTAACCCCTAACCCCTAA-3, Applied Biosystems) was added to the sections [26]. After denaturation and incubation, the relative telomere length was measured by fluorescence intensity using the TFL analysis software program [27].

Gene expression analysis

For the gene expression analysis the “Whole Mouse Genome Microarray 4x44K Array one colour” from Agilent was used [28-079]. RNA was isolated using RNazol und quality was checked using the Bioanalyzer with the “RNA 6000 Nano” from Agilent. cDNA and labelled cRNA were synthesized according to the manufacturer’s manual. Subsequently to the hybridization, the arrays were scanned by the Agilent DNA Microarray Scanner G2565CA.

Expression data were extracted using the Feature Extraction software (Agilent Technologies, Santa Clara, USA). Preprocessing of expression data was performed according to Agilent’s standard workflow. Using 5 quality flags (gIsPosAndSignif, gIsFeatNonUnifOL, gIsWellAboveBG, gIsSaturated, gIsFeatPopnOL) from the Feature Extraction software output, probes were labeled as detected, not detected, or compromised. Gene expression levels were background corrected and signals for duplicated probes were summarized by geometric mean of non-compromised probes. After log₂ transformation, a percentile shift normalization at the 75% level and a baseline shift to the median baseline of all probes was performed. All computations were done using the R statistical software framework (<http://www.R-project.org>).

Hierarchical clustering for TRF2 groups with Euclidean distance and average linkage was performed using all available probe sets and is shown as a dendrogram.

Gene set enrichment analysis was performed for a set of 880 curated canonical pathways from the Molecular Signatures Database (MSigDB) [29] as described as follows. The amount of differential expression of the individual genes (gene level statistics) was measured by Spearman correlation coefficient. The bias from using multiple probe sets targeting the same genes was adjusted by summarizing the different probe sets. The mean absolute value of

single gene statistics was used as the gene set statistic and it was compared to the Null hypothesis of no association of genes to the phenotype [30]. Computer-intensive Monte-Carlo simulation (gene sampling) was performed to assess the significance of the observed gene set statistic. Correction for multiple testing was done using the false discovery method from Benjamini and Hochberg [31]. 21 pathways were reported as significantly enriched in TTD⁺ compared to TTD⁻ (FDR < 0.05).

Venn diagram illustrating the gene overlap between enriched pathways was computed using VennMaster [32, 33].

Cross species aCGH analysis

aCGH data were extracted using the Feature Extraction software (Agilent Technologies, Santa Clara, USA). After log₂ transformation data was processed using the R-packages snapCGH and GLAD [34] to segment the data into states with the same underlying copy number. Information about known aberrations in human HCC was taken from the Progenetix database [35]. To perform an interspecies comparison between mouse and human, all genes located on aberrant chromosomal positions were extracted. The following analysis was then performed on the corresponding gene lists from TTD⁺ experiments, TTD⁻ experiments, and human HCCs.

A set of mutations given for a cancer type was divided into three parts, which are a set of random mutations, a core set of mutations common to almost all cancer types, and a cancer specific set of mutations. We calculated a minimal set of mutations that is common to most cancer types based on the information stored in the Mitelman Database of Chromosome Aberrations [36]. Mathematically, the solution to this question is the solution to the minimal set cover problem: Given a set of elements $U = \{1, \dots, n\}$ called the universe and m sets $S = \{s_1, \dots, s_m\}$ with $\bigcup s_i = U$, the optimal set cover is the minimum number of sets

$SETCOVER = \{c_i, \dots, c_k\} \in S$ with $\bigcup c_i = U$. Multiple solutions to this problem are possible.

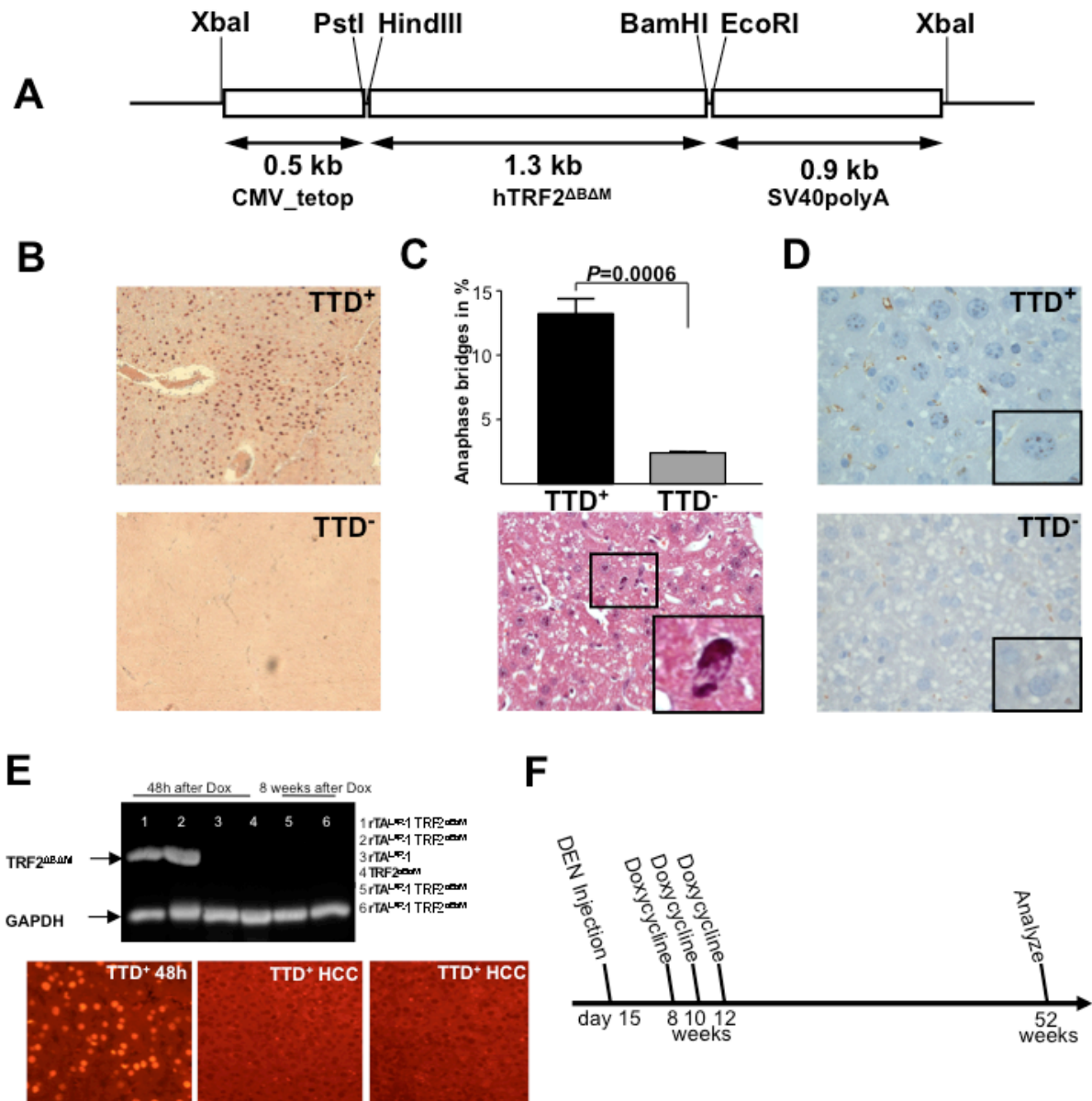
1000 different candidate solution were calculated with a greedy strategy breaking ties randomly. The set of cytobands occurring in at least one solution was used as the core set of cancer (59 cytobands).

To support the hypothesis that TTD⁺ leads to an increased HCC effect, the human HCC list containing a total of 10491 genes was corrected for HCC-unspecific mutations. At first, all genes occurring in the human HCC list and the core set of cancer were removed (3866 genes), and 4937 were found in TTD⁺ mice and 4116 were found in TTD⁻ mice. Subsequently, random mutations were filtered by only counting mutations, which are reported for at least

30% of the cases in the human HCC list (n=4777). The remaining genes (n=1848) were assigned to the groups of "at least 2 TTD⁺" or "2 TTD⁻" samples. There were 1073 genes from the filtered HCC list found in mutated regions in the TTD⁺ experiments and the TTD⁻ experiments. 333 genes were found in neither TTD⁺ nor in TTD⁻. 397 genes were found exclusively in TTD⁺ mice and 45 genes were found exclusively in TTD⁻ mice (see Suppl. figure 5). A chi-square test based on this data supports our hypothesis of more human HCC-related mutations in TTD⁺ mice ($p=2.2 \times 10^{-16}$).

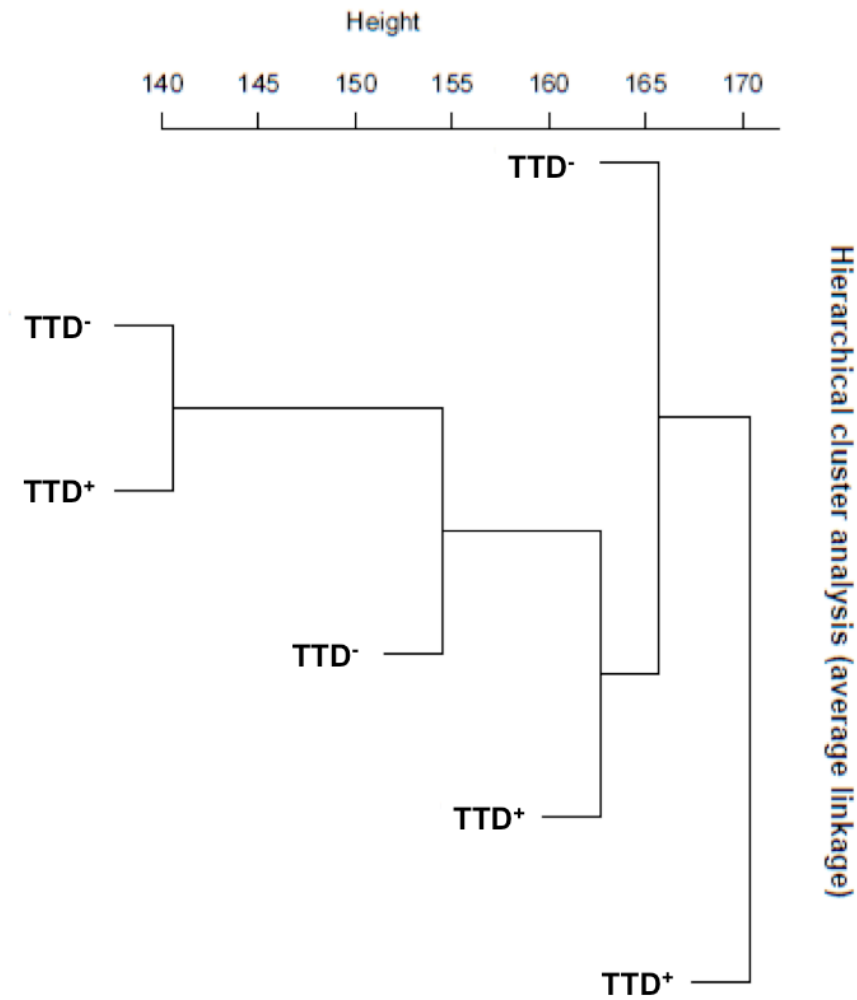
Suppl. figure 1. Intrasplesnic administration of doxycycline leads to telomeric fusions.

A. Schematic illustration of the TRF2^{ΔBΔM} tetO-inducible construct. The restriction sites used for cloning of the vector are indicated. **B.** Staining for TRF2^{ΔBΔM} showing a strong induction of protein expression in hepatocytes 24 hours after intrasplesnic doxycycline injection. (magnification: 400x) **C.** Evaluation of anaphase-bridge index 48 hours after doxycycline injection and partial hepatectomy to achieve hepatocyte proliferation revealing a significant increase in anaphase bridges ($P=0.0006$) in mice expressing TRF2^{ΔBΔM} compared to controls ($n=4$ and $n=3$ respectively) (magnification: 400x). **D.** Induction of DNA damage monitored by γ H2AX foci induced 48 hours after doxycycline treatment in TTD⁺ but not in the TTD⁻ cohort. (magnification: 630x) **E.** Western blot and immunofluorescence staining depicting the expression of the dominant-negative form of TRF2^{ΔBΔM} 48-96 hours after doxycycline administration but not leaky expression in TRF2^{ΔBΔM} single transgenic livers or TTD⁺ tumors at the time point of analysis. (magnification: 400x) **F.** Time course of the experimental setup. DEN was injected at 15 days after birth and doxycycline was administered 3 times in two-week intervals beginning at 8 weeks of age. Mice were sacrificed when they reached the age of 13 months.



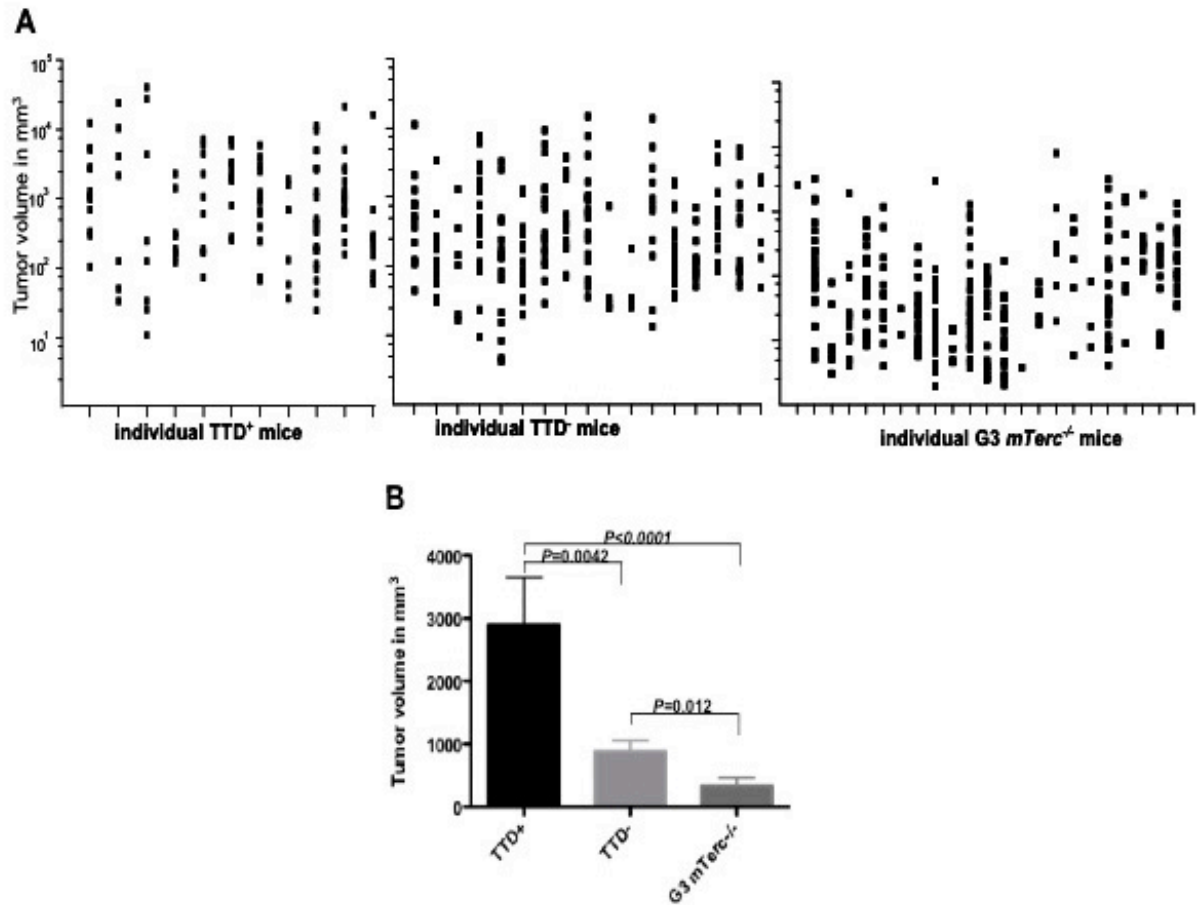
Suppl. figure 2. Hierarchical clustering reveals no global gene expression changes between *TTD*⁺ and *TTD*⁻ liver samples.

Hierarchical cluster analysis of global gene expression profiles from *TTD*⁺ and *TTD*⁻ liver (n=3) 48-72 hours after doxycycline treatment showed no specific grouping effects indicating that there were no specific patterns in gene expression separating the two groups.



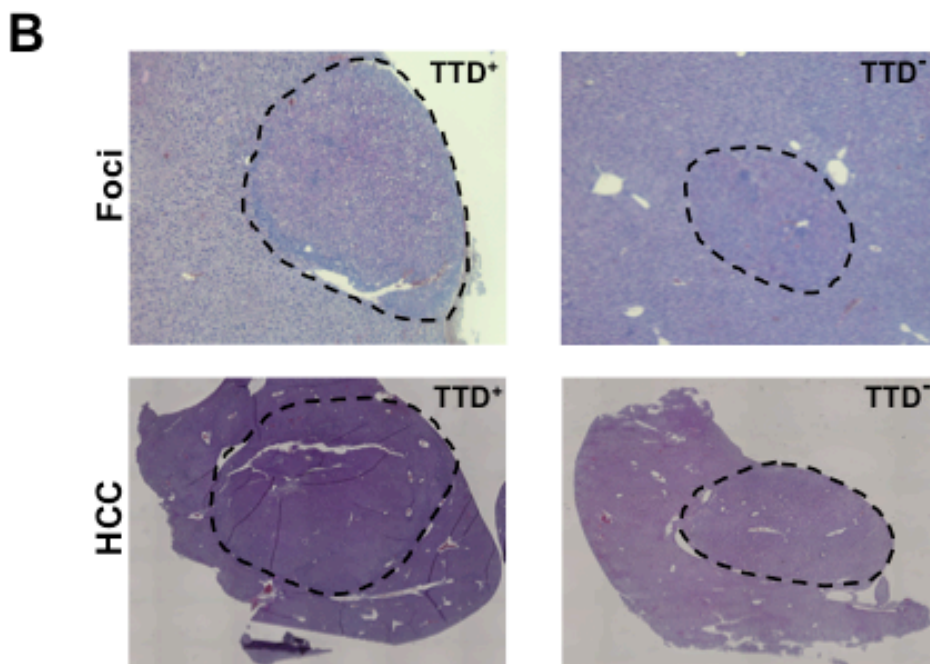
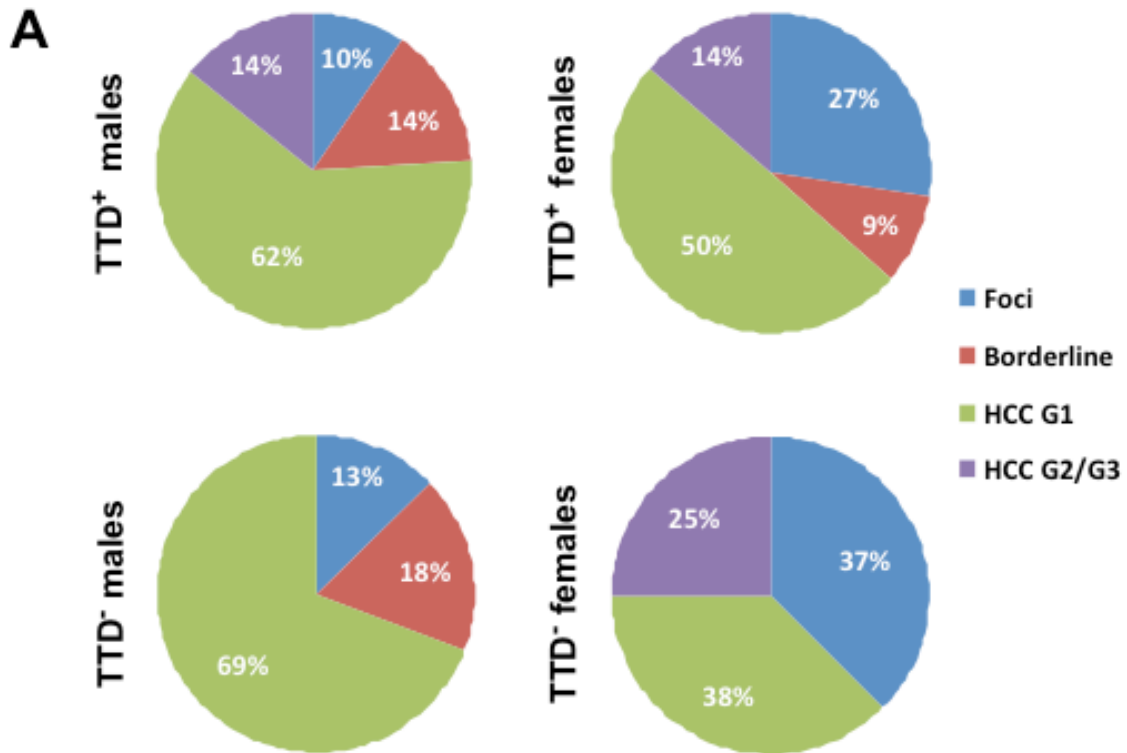
Suppl. figure 3. Statistical analysis of the tumor volume in individual mice of all cohorts.

A. The scatter blot depicts all tumor volumes determined per individual mouse of the analyzed cohorts. Note that there is a visible decrease in the tumor volume from TTD⁺ mice to TTD⁻ and *mTERC*^{-/-} G3 mice (n=11, n=17 and n=22, respectively). **B.** The bar graph displays the tumor volume normalized per analyzed mouse. Statistics reveal a significant decrease in tumor volume in TTD⁻ and *mTerc*^{-/-} G3 compared to TTD⁺ tumors ($P=0.0042$, $P<0.0001$ and $P=0.012$, respectively).



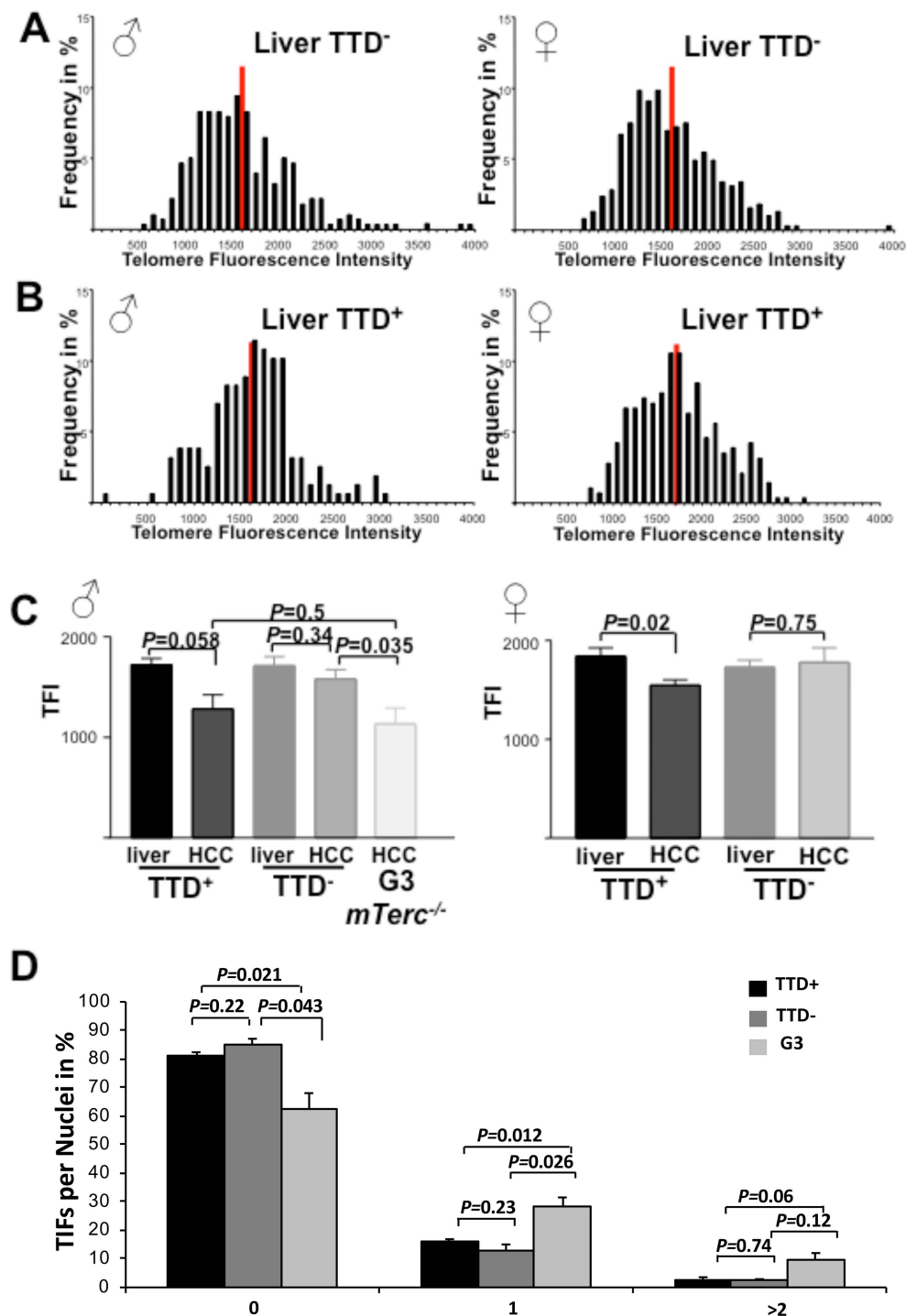
Suppl. figure 4. *Histological analysis of tumors does not reveal significant differences between genotypes.*

A Histological analysis of tumors from the indicated genotype and sex (TTD⁺ male n=21; TTD⁺ female n=22 and TTD⁻ males n=39; TTD⁻ females n=10, respectively). Tumors were histologically graded on the basis of cellular atypia and architectural complexity according to Edmondson and Steiner [37]. **B.** Representative H&E stainings of foci (magnification: 100x) and tumors (scanned at 100x magnification) of the analyzed cohorts.



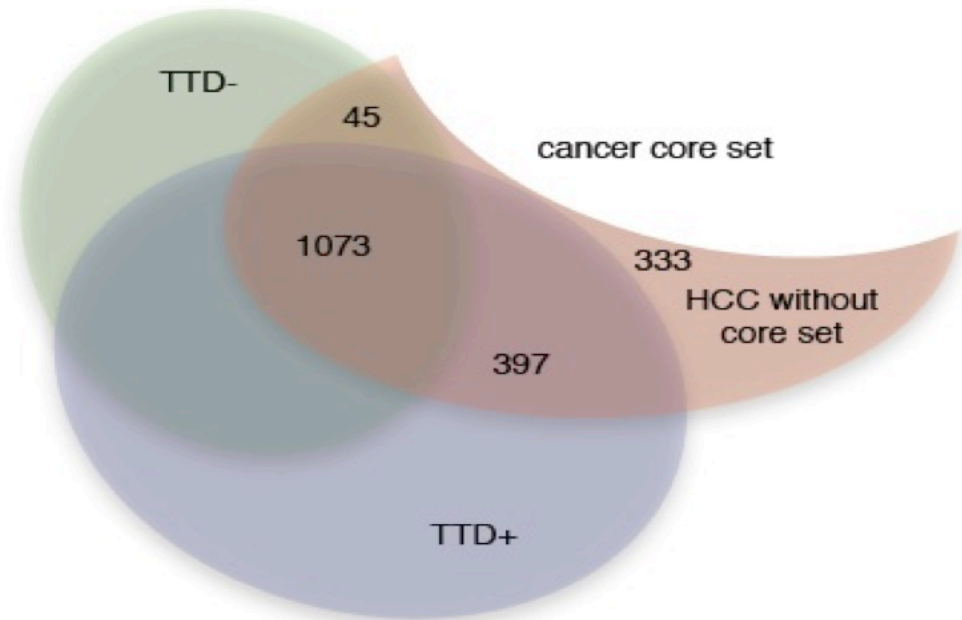
Suppl. figure 5. Transient telomere dysfunction induces HCCs with reduced telomere length.

Telomere length was measured by qFISH in hepatocytes of the indicated genotypes. **A.B.** Distribution of mean telomere fluorescence intensities (TFI) in normal liver cells of the indicated genotypes and sex (n=5-7). A red line indicates the mean fluorescence intensity of all analyzed cells. **C.** The bar graph shows the mean telomere length for each cohort and tissue. Note that the telomere length was decreased in HCCs of TTD⁺ mice. **D.** Histogram depicting the number of telomere-associated DNA damage foci (TIFs) observed in the arising tumors of the indicated cohorts. Note that TIF formation in *mTerc*^{-/-} G3 tumors is increased compared to the other cohorts indicating that the increased DNA damage is due to chronic telomere dysfunction.



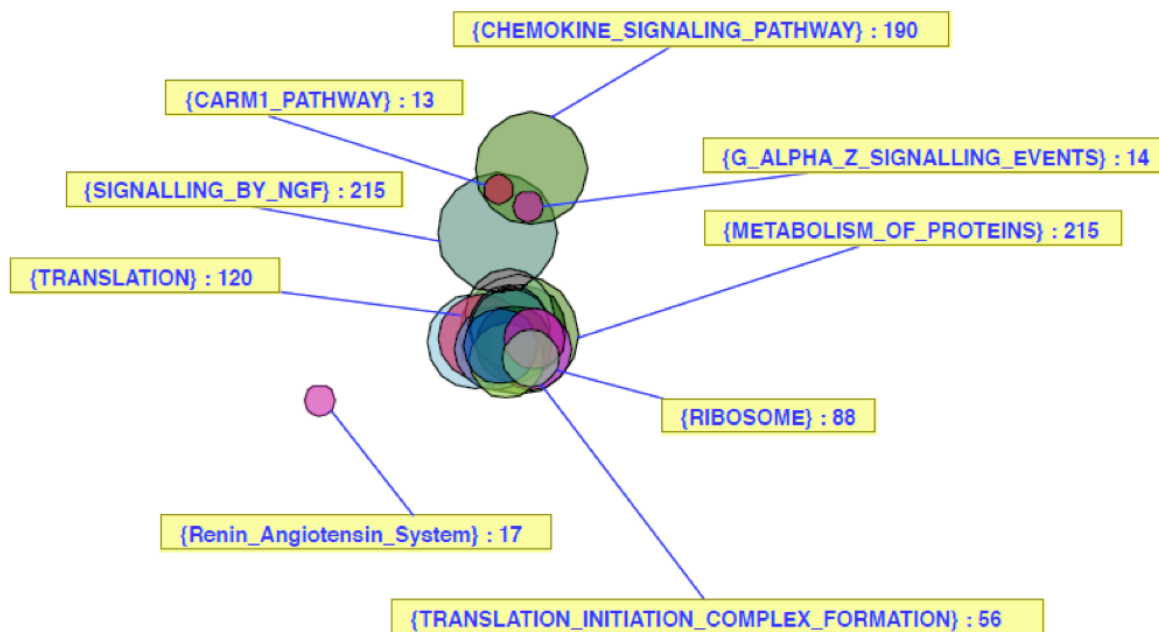
Suppl. figure 6. *Schematic representation of HCC core set of genes.*

Analysis of a core set of genes located in frequent chromosomal aberrations (gains or losses) that are specifically occurring in human HCCs. The Venn diagram analysis reveals that these genes show a higher overlap with genes located in regions of chromosomal gains or losses in TTD⁺ HCCs compared to TTD⁻ HCCs.



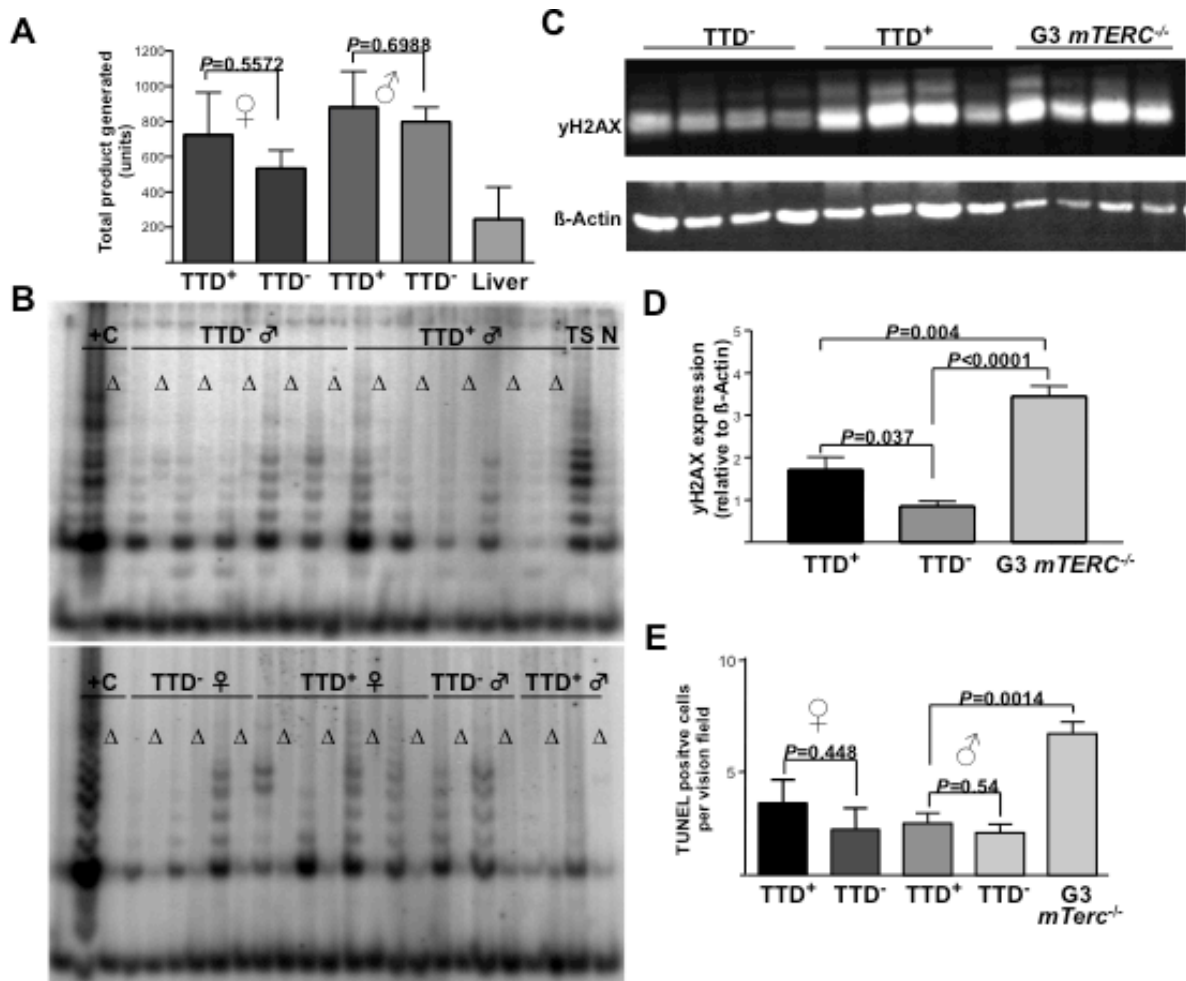
Suppl. figure 7. Venn Diagram of differentially regulated GSE-Analysis of TTD⁺ versus TTD⁻ HCCs.

Each circle represents one of 19 enriched pathways (Gene expression and Diabetes pathway are omitted due to their high number of genes). The area of a circle and its intersection is proportional to the number of genes involved in a pathway. An overlap of two circles shows the intersection in the number of genes in two pathways. Most of the enriched pathways share the majority of genes, whereas 5 pathways (Carm1, G alpha Z signalling events, Renin angiotensin system, Chemokine signalling, Signalling by NGF) contribute a differing gene signature. Note the strong enrichment for pathways involved in ribosomal gene translation – a known process associated with tumor formation.



Suppl. figure 8. Transient expression of $TRF2^{\Delta BAM}$ does not lead to a difference in telomerase activity but leads to increased activation of the DNA-damage signalling cascade.

A. Histogram displaying the mean telomerase activity of all HCC tumors analyzed (total product generated [units], n=3-7). **B.** Representative TRAP pictures of extracts isolated from HCCs of different genotypes. Telomerase activity of different intensity can be detected in all tumors from both cohorts (Δ signifies heat-inactivated samples). **C.** Representative western blot of γ H2AX using β -Actin as a loading control from protein samples of the indicated cohorts. The lanes were run on the same gel, but were noncontiguous. **D.** The degree of γ H2AX phosphorylation was analysed using the β -Actin as a loading control and the mean of different samples is plotted in the bar graph. **E.** The bar graph displays the number of TUNEL-positive cells analyzed in HCC tumors of the different cohorts per vision field (n=3-6). Note that the overall level of apoptosis is low in tumors of both groups.



Suppl. Table 1. Differentially regulated GSEA pathways of TTD⁺ HCCs are implicated in human hepatocarcinogenesis. The table displays the GSEA pathways, which are significantly differentially regulated in TTD⁺ versus TTD⁻ tumors (n=3). Literature search of involved genes and pathways revealed that all of the pathways were reported to be involved in human hepatocarcinogenesis (see references in right column).

GSEA pathways	Significance TTD⁻ vs. TTD⁺	References
KEGG_Ribosome	0,0052	Hruban, 1979 (38)
KEGG_Chemokine Signaling Pathway	0,0052	Anson 2012 (39)
KEGG_Renin Angiotensin System	0,0251	Yoshiji 2011 (40)
BIOCARTA_Carm1 Pathway	0,0139	Al-Dhaheer 2011 (41)
REACTOME_Diabetes Pathway	0,0052	Evert 2012 (42); Yang 2011 (43)
REACTOME_Formation of ternary complex and the 43S complex	0,0052	Robert 2006 (44)
REACTOME_G-alpha-Z-signaling events	0,0098	Kimple 2008 (45)
REACTOME_Insulin synthesis and secretion	0,0052	Breuhahn 2008 (46)
REACTOME_Metabolism of proteins	0,0052	Zhou 1998 (47)
REACTOME_Peptide chain elongation	0,0052	Roy 2010 (48)
REACTOME_Regulation of beta cell development	0,0052	Pajvani 2011 (49)
REACTOME_Regulation of gene expression in beta cells	0,0052	Green 2009 (50)
REACTOME_Signalling by NGF	0,0176	Tokusashi 2005 (51)
REACTOME_Translation	0,0052	Shuda 2000 (52)
REACTOME_Translation initiation complex formation	0,0052	Lim 2011 (53)

References

26. Lechel A, et al. Telomerase deletion limits progression of p53-mutant hepatocellular carcinoma with short telomeres in chronic liver disease. *Gastroenterology*. 2007;132(4):1465-75.
27. Poon SS, Martens UM, Ward RK, Lansdorp PM. Telomere length measurements using digital fluorescence microscopy. *Cytometry*. 1999;36(4):267-78.
28. Badvie S. Hepatocellular carcinoma. *Postgrad Med J*. 2000;76(891):4-11.
29. Subramanian A, et al. Gene set enrichment analysis: a knowledge-based approach for interpreting genome-wide expression profiles. *Proceedings of the National Academy of Sciences of the United States of America*. 2005;102(43):15545-50.
30. Ackermann M, Strimmer K. A general modular framework for gene set enrichment analysis. *BMC Bioinformatics*. 2009;10:47.
31. Benjamini Y, Hochberg Y. Controlling the false discovery rate: A practical and powerful approach to multiple testing. *Journal of the Royal Statistical Society, Series B* 1995;57(1):289-300.
32. Kestler HA, Muller A, Gress TM, Buchholz M. Generalized Venn diagrams: a new method of visualizing complex genetic set relations. *Bioinformatics*. 2005;21(8):1592-5.
33. Kestler HA, et al. VennMaster: area-proportional Euler diagrams for functional GO analysis of microarrays. *BMC Bioinformatics*. 2008;9:67.
34. Hupe P, Stransky N, Thiery JP, Radvanyi F, Barillot E. Analysis of array CGH data: from signal ratio to gain and loss of DNA regions. *Bioinformatics*. 2004;20(18):3413-22.
35. Baudis M, Cleary ML. Progenetix.net: an online repository for molecular cytogenetic aberration data. *Bioinformatics*. 2001;17(12):1228-9.
36. Mitelman F, Johansson B, Mertens F. Mitelman Database of Chromosome Aberrations and Gene Fusions in Cancer.; 2011. Available at: <http://cgap.nci.nih.gov/Chromosomes/Mitelman>.
37. Edmondson HA, Steiner PE. Primary carcinoma of the liver: a study of 100 cases among 48,900 necropsies. *Cancer*. 1954;7(3):462-503.
38. Hruban Z. Ultrastructure of hepatocellular tumors. *J Toxicol Environ Health*. 1979;5(2-3):403-33.
39. Anson M, et al. Oncogenic beta-catenin triggers an inflammatory response that determines the aggressiveness of hepatocellular carcinoma in mice. *J Clin Invest*. 2012;122(2):586-99.
40. Yoshiji H, Noguchi R, Ikenaka Y, Kaji K, Aihara Y, Fukui H. Impact of renin-angiotensin system in hepatocellular carcinoma. *Curr Cancer Drug Targets*. 2011;11(4):431-41.
41. Al-Dhaheri M, et al. CARM1 is an important determinant of ERalpha-dependent breast cancer cell differentiation and proliferation in breast cancer cells. *Cancer research*. 2011;71(6):2118-28.
42. Evert M, et al. AKT/mTOR activation induces a module of metabolic changes contributing to growth in insulin-induced hepatocarcinogenesis. *Hepatology*. 2012.
43. Yang WS, et al. The role of pre-existing diabetes mellitus on hepatocellular carcinoma occurrence and prognosis: a meta-analysis of prospective cohort studies. *PloS one*. 2011;6(12):e27326.
44. Robert F, et al. Initiation of protein synthesis by hepatitis C virus is refractory to reduced eIF2.GTP.Met-tRNA(i)(Met) ternary complex availability. *Mol Biol Cell*. 2006;17(11):4632-44.
45. Kimple ME, et al. Galphaz negatively regulates insulin secretion and glucose clearance. *J Biol Chem*. 2008;283(8):4560-7.

46. Breuhahn K, Schirmacher P. Reactivation of the insulin-like growth factor-II signaling pathway in human hepatocellular carcinoma. *World J Gastroenterol*. 2008;14(11):1690-8.
47. Zhou J, et al. A novel transcription factor, ELF5, belongs to the ELF subfamily of ETS genes and maps to human chromosome 11p13-15, a region subject to LOH and rearrangement in human carcinoma cell lines. *Oncogene*. 1998;17(21):2719-32.
48. Roy L, et al. Proteomic analysis of the transitional endoplasmic reticulum in hepatocellular carcinoma: an organelle perspective on cancer. *Biochim Biophys Acta*. 2010;1804(9):1869-81.
49. Pajvani UB, et al. Inhibition of Notch signaling ameliorates insulin resistance in a FoxO1-dependent manner. *Nat Med*. 2011;17(8):961-7.
50. Green CD, Jump DB, Olson LK. Elevated insulin secretion from liver X receptor-activated pancreatic beta-cells involves increased de novo lipid synthesis and triacylglyceride turnover. *Endocrinology*. 2009;150(6):2637-45.
51. Tokusashi Y, et al. Expression of NGF in hepatocellular carcinoma cells with its receptors in non-tumor cell components. *International journal of cancer Journal international du cancer*. 2005;114(1):39-45.
52. Shuda M, et al. Enhanced expression of translation factor mRNAs in hepatocellular carcinoma. *Anticancer Res*. 2000;20(4):2489-94.
53. Lim KH, et al. RPS3a over-expressed in HBV-associated hepatocellular carcinoma enhances the HBx-induced NF-kappaB signaling via its novel chaperoning function. *PloS one*. 2011;6(8):e22258.